

# UNCLASSIFIED

AD NUMBER
ADB244931
NEW LIMITATION CHANGE
TO Approved for public release, distribution unlimited
FROM Distribution authorized to U.S. Gov't. agencies only; Proprietary Info.; Sep 98. Other requests shall be referred to U.S. Army Medical Research and Materiel Command, 504 Scott St., Fort Detrick, MD 21702-5012.
AUTHORITY
USAMRMC ltr, 23 Aug 2001

THIS PAGE IS UNCLASSIFIED

AD \_\_\_\_\_

GRANT NUMBER DAMD17-97-1-7079

TITLE: NMR Reconstructive Elasticity Imaging of Breast:  
Surrogate Remote Palpation Using Quantitative 3-D Displacement  
and Strain Estimations

PRINCIPAL INVESTIGATOR: Thomas L. Chenevert, Ph.D.

CONTRACTING ORGANIZATION: University of Michigan  
Ann Arbor, Michigan 48109

REPORT DATE: September 1998

TYPE OF REPORT: Annual

PREPARED FOR: U.S. Army Medical Research and Materiel Command  
Fort Detrick, Maryland 21702-5012

DISTRIBUTION STATEMENT: Distribution authorized to U.S. Government agencies only (proprietary information, Sep 98). Other requests for this document shall be referred to U.S. Army Medical Research and Materiel Command, 504 Scott Street, Fort Detrick, Maryland 21702-5012.

The views, opinions and/or findings contained in this report are those of the author(s) and should not be construed as an official Department of the Army position, policy or decision unless so designated by other documentation.

**DTIC QUALITY INSPECTED 4**

## NOTICE

USING GOVERNMENT DRAWINGS, SPECIFICATIONS, OR OTHER DATA INCLUDED IN THIS DOCUMENT FOR ANY PURPOSE OTHER THAN GOVERNMENT PROCUREMENT DOES NOT IN ANY WAY OBLIGATE THE U.S. GOVERNMENT. THE FACT THAT THE GOVERNMENT FORMULATED OR SUPPLIED THE DRAWINGS, SPECIFICATIONS, OR OTHER DATA DOES NOT LICENSE THE HOLDER OR ANY OTHER PERSON OR CORPORATION; OR CONVEY ANY RIGHTS OR PERMISSION TO MANUFACTURE, USE, OR SELL ANY PATENTED INVENTION THAT MAY RELATE TO THEM.

### LIMITED RIGHTS LEGEND

Award Number: DAMD17-97-1-7079

Contractor: University of Michigan

Location of Limited Rights Data (Pages): 7-9;11-13

Those portions of the technical data contained in this report marked as limited rights data shall not, without the written permission of the above contractor, be (a) released or disclosed outside the government, (b) used by the Government for manufacture or, in the case of computer software documentation, for preparing the same or similar computer software, or (c) used by a party other than the Government, except that the Government may release or disclose technical data to persons outside the Government, or permit the use of technical data by such persons, if (i) such release, disclosure, or use is necessary for emergency repair or overhaul or (ii) is a release or disclosure of technical data (other than detailed manufacturing or process data) to, or use of such data by, a foreign government that is in the interest of the Government and is required for evaluational or informational purposes, provided in either case that such release, disclosure or use is made subject to a prohibition that the person to whom the data is released or disclosed may not further use, release or disclose such data, and the contractor or subcontractor or subcontractor asserting the restriction is notified of such release, disclosure or use. This legend, together with the indications of the portions of this data which are subject to such limitations, shall be included on any reproduction hereof which includes any part of the portions subject to such limitations.

THIS TECHNICAL REPORT HAS BEEN REVIEWED AND IS APPROVED FOR PUBLICATION.

Patricia Madison

6/4/99

REPORT DOCUMENTATION PAGE			Form Approved OMB No. 0704-0188	
Public reporting burden for this collection of information is estimated to average 1 hour per response, including the time for reviewing instructions, searching existing data sources, gathering and maintaining the data needed, and completing and reviewing the collection of information. Send comments regarding this burden estimate or any other aspect of this collection of information, including suggestions for reducing this burden, to Washington Headquarters Services, Directorate for Information Operations and Reports, 1215 Jefferson Davis Highway, Suite 1204, Arlington, VA 22202-4302, and to the Office of Management and Budget, Paperwork Reduction Project (0704-0188), Washington, DC 20503.				
1. AGENCY USE ONLY (Leave blank)		2. REPORT DATE September 1998		3. REPORT TYPE AND DATES COVERED Annual (11 Aug 97 - 10 Aug 98)
4. TITLE AND SUBTITLE NMR Reconstructive Elasticity Imaging of Breast: Surrogate Remote Palpation Using Quantitative 3-D Displacement and Strain Estimations			5. FUNDING NUMBERS DAMD17-97-1-7079	
6. AUTHOR(S) Chenevert, Thomas L., Ph.D.				
7. PERFORMING ORGANIZATION NAME(S) AND ADDRESS(ES) University of Michigan Ann Arbor, Michigan 48109			8. PERFORMING ORGANIZATION REPORT NUMBER	
9. SPONSORING / MONITORING AGENCY NAME(S) AND ADDRESS(ES) U.S. Army Medical Research and Materiel Command Fort Detrick, Maryland 21702-5012			10. SPONSORING / MONITORING AGENCY REPORT NUMBER	
11. SUPPLEMENTARY NOTES			19990622 040	
12a. DISTRIBUTION / AVAILABILITY STATEMENT Distribution authorized to U.S. Government agencies only (proprietary information, Sep 98). Other requests for this document shall be referred to U.S. Army Medical Research and Materiel Command, 504 Scott Street, Fort Detrick, Maryland 21702-5012.			12b. DISTRIBUTION CODE	
13. ABSTRACT (Maximum 200 words) The goal of this research program is to develop a sensitive diagnostic technique based on quantitative elasticity imaging permitting surrogate palpation of deep lying breast lesions. The remote measurement of elasticity in breast tissues may provide unique information which could increase detection and/or characterization of potentially malignant masses not accessible to manual palpation. The primary technical objective of this study is to refine and test a novel MRI method for the acquisition of high resolution 3-dimensional spatial displacement data through the imaged object for quantitative estimation of internal strain and elastic modulus. Proof-of-concept of the proposed 3D displacement-encoding, stimulated echo technique has been completed and recently published using two-dimensional test objects. Design, fabrication, and refinement of an MRI pulse-sequence controlled, pneumatic deformation device is now complete. Initial tests confirm this device provides highly reproducible deformations as required by the method. Stable phantom materials and fabrication procedures have been determined for production of test objects. Extension of elasticity reconstruction and boundary detection algorithms to accommodate dimensionality of the MRI data are underway, with initial 3D-phantom tests planned for the first quarter of project year#2.				
14. SUBJECT TERMS Breast Cancer			15. NUMBER OF PAGES 26	
			16. PRICE CODE	
17. SECURITY CLASSIFICATION OF REPORT Unclassified	18. SECURITY CLASSIFICATION OF THIS PAGE Unclassified	19. SECURITY CLASSIFICATION OF ABSTRACT Unclassified	20. LIMITATION OF ABSTRACT Limited	

## FOREWORD

Opinions, interpretations, conclusions and recommendations are those of the author and are not necessarily endorsed by the U.S. Army.

NA Where copyrighted material is quoted, permission has been obtained to use such material.

NA Where material from documents designated for limited distribution is quoted, permission has been obtained to use the material.

JK Citations of commercial organizations and trade names in this report do not constitute an official Department of Army endorsement or approval of the products or services of these organizations.

NA In conducting research using animals, the investigator(s) adhered to the "Guide for the Care and Use of Laboratory Animals," prepared by the Committee on Care and use of Laboratory Animals of the Institute of Laboratory Resources, national Research Council (NIH Publication No. 86-23, Revised 1985).

NA For the protection of human subjects, the investigator(s) adhered to policies of applicable Federal Law 45 CFR 46.

NA In conducting research utilizing recombinant DNA technology, the investigator(s) adhered to current guidelines promulgated by the National Institutes of Health.

NA In the conduct of research utilizing recombinant DNA, the investigator(s) adhered to the NIH Guidelines for Research Involving Recombinant DNA Molecules.

NA In the conduct of research involving hazardous organisms, the investigator(s) adhered to the CDC-NIH Guide for Biosafety in Microbiological and Biomedical Laboratories.

Thomas J. Bennett 2/9/88  
PI - Signature Date

<b><u>TABLE OF CONTENTS</u></b>	<b><u>Page</u></b>
<b>INTRODUCTION</b>	<b>2 - 3</b>
<b>METHODS AND RESULTS PER TASK</b>	<b>3 - 11</b>
<b>CONCLUSIONS</b>	<b>11</b>
<b>REFERENCES</b>	<b>12 - 14</b>

**APPENDIX**

Reprint of: "Elasticity reconstructive imaging via stimulated echo MRI,"  
T.L. Chenevert, A.R. Skovoroda, M. O'Donnell, and S.Y. Emelianov,  
Magnetic Resonance in Medicine, 39, pp. 482-490 (1998).

## INTRODUCTION

Manual palpation remains the first diagnostic line of defense against breast cancer. Whether performed in a self-examination or clinical physical exam, breast palpation is a low cost, totally non-invasive test that often is the initial means of disease detection [1-4]. Unfortunately, physical examination of the breast has many limitations including variable skill of the examiner (particularly for breast self-exams) and subjectivity. Perhaps its greatest limitation, however, is that sensitivity to palpate masses deep in the breast, or within relatively dense, stiff, or heterogeneous tissues, is poor. The principal objective of this project is to develop a means to measure/image tissue elasticity (i.e., "hardness") deep within tissues. The hypothesis is that remote measurement of elasticity in breast tissues is possible and provides unique information, which could increase detection and/or characterization of potentially malignant masses not accessible to manual palpation. Our preliminary studies suggest that the proposed methods are capable of precisely measuring internal deformation and strain in three dimensions. These data are required to reconstruct the elasticity distribution within the object. Consequently, technologies developed within the scope of this project may have significant diagnostic value in detection and management of breast cancer.

Imaging scientists have attempted to electronically extend the touch of the physical examiner by a variety of techniques that infer tissue elasticity. The essential element of these approaches is to measure relative internal motion and strain of tissue structures experiencing mechanical stress. Most elastography to date has utilized ultrasound [5-14], although MRI has also been used [15-22]. Usually an external static or dynamic deformation is applied while the resultant displacement or propagating shear wave is documented by imaging devices. In the original MRI method, spatial magnetization tagging was applied, but this had poor spatial sampling of displacement and only measured 2-D motion [18]. More recently, motion phase encoding via bi-polar gradients was employed to produce 2-D strain maps in media mechanically driven by external forces [19-22]. This approach is applicable to measure quasi-static displacement or dynamically record propagation of mechanical shear waves and produce strain images. While strain depends on internal elastic properties, it is also strongly affected by the applied deformational geometry, and thus is not uniquely reflective of tissue properties (i.e., Young's modulus). "Dynamic" measurements exhibit local shear wavelength, which allow direct calculation of Young's modulus. Shear wave attenuation, interference from standing waves off multiple reflectors, and limited resolvable points over the shear wavelength are significant challenges being address by investigators of these methods.

Relative to ultrasound, nuclear magnetic resonance (NMR) imaging (MRI) has two major advantages for elasticity imaging. First, the resolution and accuracy of NMR displacement and strain components can be isotropic compared to ultrasound estimates. Indeed, ultrasound can accurately measure axial (i.e., along the beam axis) motion at high spatial resolution ( $\leq 1\text{mm}$ ), but lateral displacement is measurable at much lower spatial resolution defined by the acoustic beam width which varies with depth. The third dimension is generally not even considered given the limitations of ultrasound. Consequently, the "elastogram" is compromised by reduced motion dimensionality and overall low motion resolution of the imaging system. In MRI, isotropic resolution of  $\approx 1\text{mm}$  can be readily achieved by standard means. Secondly, NMR displacement and strain estimates are less sensitive to the strain decorrelation effects that produce substantial error in ultrasound cross-correlation speckle motion estimates. Indeed, large

strains change the spatial distribution of the speckle patterns used for motion tracking markedly increasing errors in displacement and strain estimates [13, 14]. This would have a significant impact on the signal-to-noise (SNR) of the NMR displacement, strain, and, subsequently, elasticity images.

Limitations of the imaging modality notwithstanding, the theoretical framework to derive elasticity using 2-D and 3-D motion models have initially been developed by members of our group [24-26]. We have also developed an algorithm to uniquely reconstruct spatial maps of Young's modulus from 1-dimensional estimates of internal displacement and strain as often done in ultrasound elasticity imaging. The algorithm has been verified using two-dimensional phantoms and a unique method of ultrasound displacement and strain imaging. Limited lateral resolution of the acoustic imaging system meant only one component of the displacement vector was measured, but this was sufficient given the phantom geometry to reconstruct maps of Young's modulus.

In general, to reconstruct the tissue-specific property of Young's modulus in complex systems such as the breast, the full 3-D displacement vector must be measured over a 3-D volume. To date, no group has attempted this by any imaging modality. In this project, we will develop the techniques that can measure the 3-D displacement vector over any volume in the object. These data will be processed to produce 3-D strain images and allow reconstruction of Young's modulus over the volume. It should be feasible to translate these methods to image the breast in a clinical setting.

## **METHODS AND RESULTS IN RELATION TO STATEMENT OF WORK**

The goal of this research program is to develop a sensitive diagnostic technique based on quantitative elasticity imaging permitting surrogate palpation of deep lying breast lesions. The underlying hypothesis in this project is that measurement of elasticity in breast tissues provides unique information that could increase detection and/or characterization of potentially malignant masses not accessible to manual palpation. The purpose of this study is to develop technology for acquisition of high resolution 3-D MRI spatial and displacement data through the breast for calculation of strain and elastic modulus images. To this end, specific technical objectives/tasks were adopted and summarized in the proposal Statement of Work. Each task is restated below along with descriptions of relevant Methods and Progress/Results.

### **Technical Objective I: Data Acquisition and Reconstruction**

#### **Task 1: Month 1-3**

*Construction of computer controlled hydraulic compression device capable of producing an incremental surface deformation of the mechanical body. This device will be triggered by NMR imaging system and have a simple timing/displacement control appropriate for phantom studies.*

The proposed method requires that the imaged object experience a relatively minor externally-applied deformation force. Based on signal optimization simulations (described below), differential deformations below 10% should be adequate to generate elasticity maps (e.g., <1cm deformation across a 10cm object). A drawback, however, of phase-encode methods employed here is that data are acquired in many segments over an extended period of time (minutes); thus, the mechanical deformation must be reproduced

for each segment. We designed the acquisition sequence to be insensitive to inevitable, ill-defined motions (vibrations) during deformation transitions, but the endpoint of each mechanical transition needs to be highly reproducible. Clearly, design and fabrication of the compression device is a critical prerequisite to phantom studies. Development of this device dominated the first 10 months of this project.

For electrical safety and handling ease, hydraulics were abandoned early in the design process for pneumatic drives. A high capacity >40psi air source piped into the NMR laboratory was available to drive the device. Our first automated deformation system held the tissue-mimicking phantom between two horizontal plates. A pneumatic bladder above the top plate was used to apply an incremental vertical deformation force and mechanical "stops" on guide posts were set to define deformation limits. Upon release of air pressure in the bladder, the phantom would passively recoil to its initial

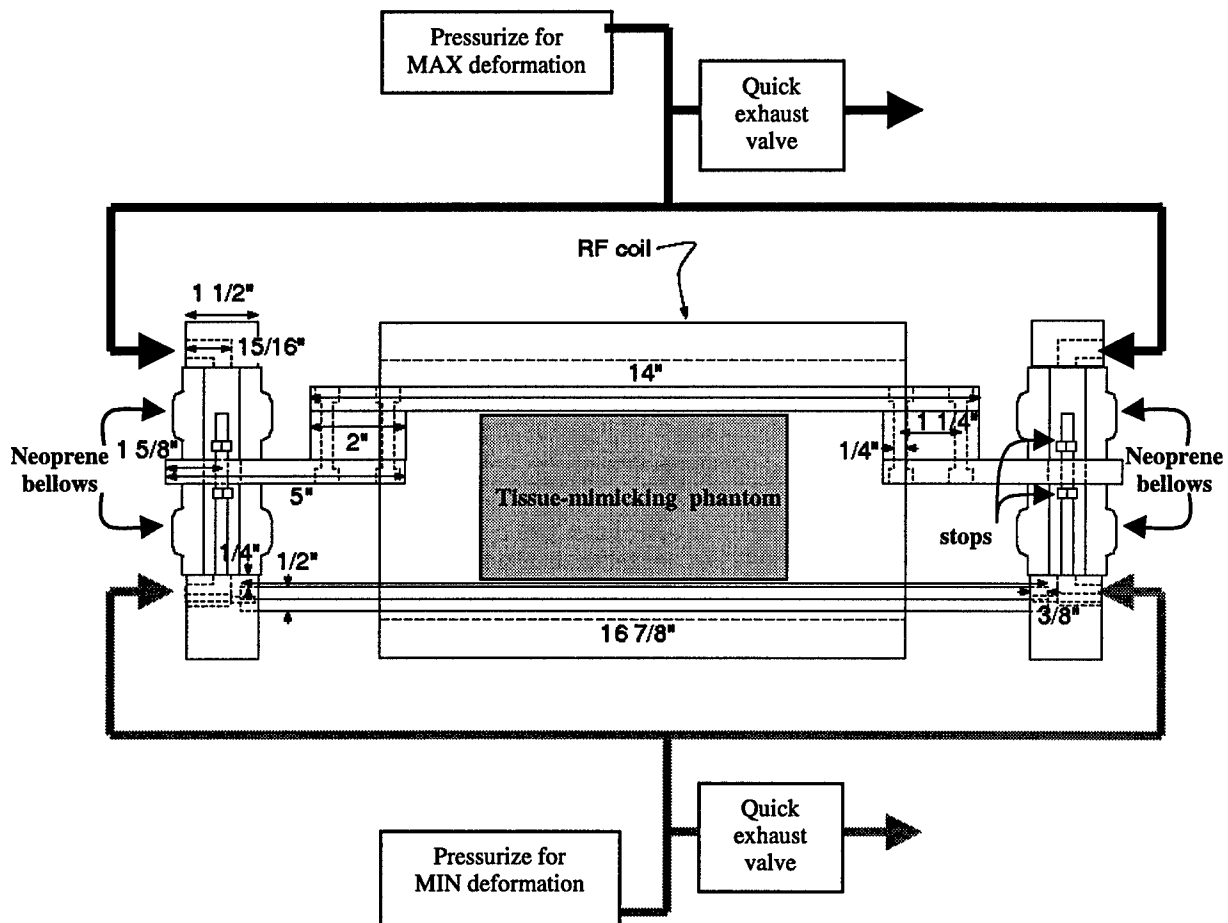


**Figure 1. Side-view schematic of pneumatic deformation system.**

state. While successful for initial proof-of-concept studies [27, 28], we realized that a system based on "passive recoil" was inadequate since the recoil time itself was dependent on viscoelastic properties of the object and the degree of applied deformation, thus this timing would be difficult to control.

Our second generation device employed active deformation and active recoil. Machinist specifications and pneumatic logic for the device are shown in Figure 1. Four neoprene bellows outside of the NMR coil (rf-coil) provide both upward and downward force to an acrylic plate on top of the phantom. The top bellows are on a common pressure circuit, likewise the bottom pair are pressurized together to yield uniform vertical displacement along the top of phantom. Solid acrylic yolks at both ends of the device insure that only the top plate moves in response to pressurization. Tests on a variety of bellow sizes/designs led to current configuration of 2.2" diameter neoprene expansion-joint boots with an additional rigid sleeve around each boot to keep expansion

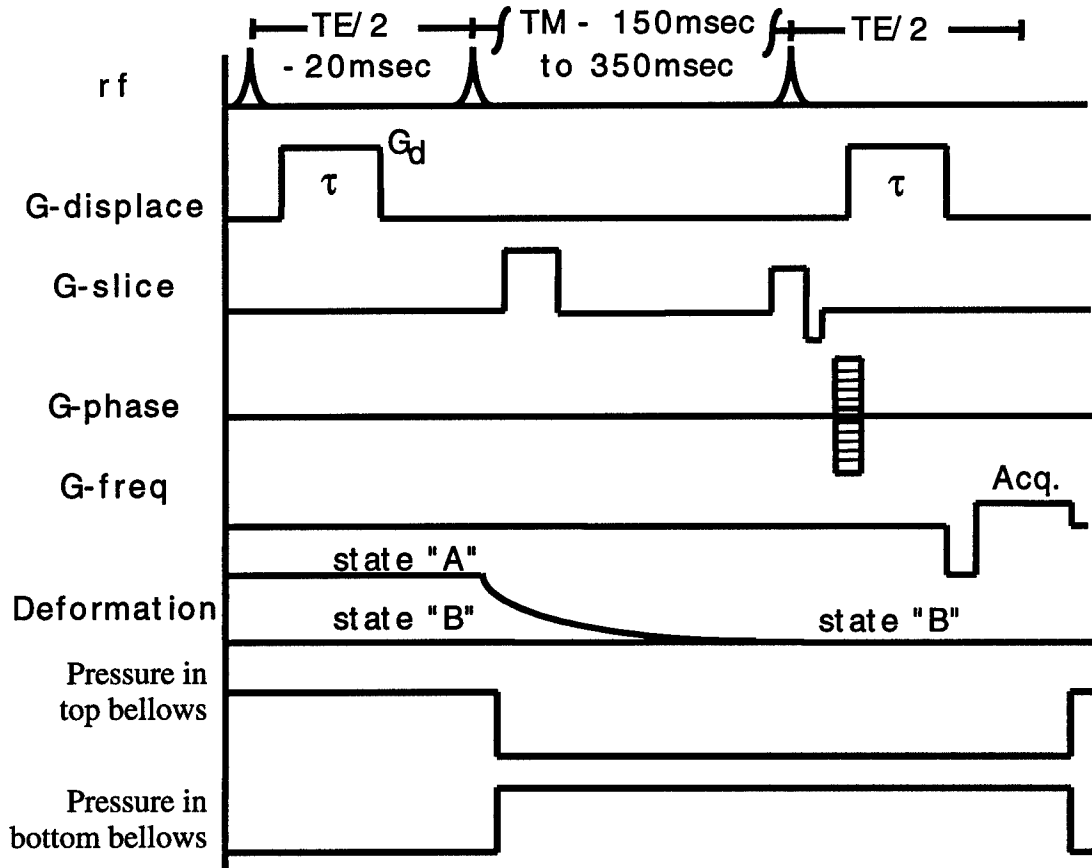


**Figure 2. Stimulated-echo data acquisition and deformation sequence. Mechanical transitions occur during the relatively long mixing time  $T_M$ . A sequence-triggered TTL circuit controls pneumatic relays to pressurize for active deformation and recoil.**

forces vertical. Further testing revealed that while only one pair of bellows (top or bottom) were pressurized at any one time, the residual pressure in the opposing bellows greatly slowed the response of the system to change deformation state. There is a signal-to-noise advantage to rapidly switch between deformation states. Quick exhaust valves for each bellow pair were added to substantially improve system response time. These valves provide rapid equalization to atmosphere soon after pressure starts to drop in the bellows.

Mechanical stability tests of the device were performed using a slightly modified version of the 2D-displacement encoding MRI sequence illustrated in Figure 2.

Displacement encoding pulses (Gd) were set to  $3.8\pi/\text{mm}$  -  $15.3\pi/\text{mm}$  sensitivity along horizontal and vertical directions. The deformation device was loaded with a tissue-mimicking phantom, and repeated runs (128 echoes) were acquired without phase encoding (i.e., G-phase=0) such that phase variations in observed echoes would reflect mechanical instability. For example, assuming a displacement sensitivity of  $3.8\pi/\text{mm}$ , a measured phase instability of  $0.38\pi$  would suggest a mechanical instability of 0.1mm. The upshot of these tests was that the system is extremely stable and reproducible in application of a 5mm differential deformation (mixing time,  $T_M=350\text{msec}$ ). The observed phase instabilities were barely above that allowed by NMR signal limits. These results suggest mechanical reproducibility within  $<20\text{microns}$ . Additional tests are planned to determine stability at shorter mixing times of  $T_M=100$  to  $250\text{msec}$ .

## Task 2: Month 1-6

*Development of various phantoms to test NMR displacement and strain data acquisition and 3-D elasticity reconstruction algorithms.*

Fabrication of phantoms to model the mechanical and NMR properties of human tissue is an important step in development and verification of optimized NMR displacement-encoded, volume simulated-echo pulse sequence, and elasticity reconstruction algorithms. The phantom materials, therefore, should closely resemble relevant tissue properties. In addition, these materials should be stable (i.e., material properties should not change over sufficiently long periods of time) and permit the non-destructive embedding of tissue specimen into the phantom.

We have previously developed tissue-mimicking phantoms to test NMR elasticity imaging device. These phantoms were made of two materials: a) polymer produced by M-F Manufacturing Co., Inc. (Fort Worth, TX), and b) gelatin (Sigma-Aldrich Co., 3050 Spruce Street, St. Louis, MO 63103 USA). The first material, plastisol, consists of a liquid plastic combined with either softener (plasticizer) or hardener. By varying the proportion of these two components, it is possible to produce composite models of desired elasticity. The raw composite materials were stirred and heated to approximately  $170^\circ\text{C}$ . At that temperature the mixture was poured into molds producing a tissue-mimicking time-stable phantom of desired shape and elasticity distribution. However, two major deficiencies remain. First, plastisol does not have desired tissue equivalent NMR properties. Second, due to high temperature rise during phantom preparation, it is impossible to produce tissue-containing phantoms using plastisol.

Gelatin phantoms can mimic both elastic and NMR properties of tissue as well. In addition, gelatin preparation procedures allow fabrication of tissue-containing phantoms, but these phantoms cannot be kept over a long period of time. Moreover, elastic properties of gelatin phantoms are highly unstable.

Several different materials were further considered for NMR elasticity phantoms. These materials include Semicosil 921, Semicosil 905 and Silgel 612 (Wacker Silicones Co., Adrian, MI 49221), and Rhodorsil RTV 163 (Rhone-Poulenc, France). From all tested materials, the Semocosil 921 silicone gel appeared to mimic the tissue properties the best. The elasticity of silicone gel can be simply controlled by mixing ratio of two components. The composite material is then poured into the mold and cured at the room temperature enabling fabrication of tissue containing phantoms. These silicone gels have shown high SNR spin-echo signal over the range of hardness variations. In addition, the mechanical properties of silicone did not change over 60 days, as was measured by

Instron-type mechanical system. Therefore, it is possible to fabricate tissue-mimicking phantoms of desired shape and elasticity distribution using Semicosil 921 silicone gel.

### **Task 3: Month 1-12**

*Development of the NMR displacement-encoded, volume simulated-echo pulse sequence optimized for displacement/strain sensitivity and SNR.*

There are several positive features in our displacement-encoding stimulated-echo sequence which are particularly well suited to elasticity imaging. Difficulties encountered with "dynamic" methods to document shear-wave propagation are avoided by the employed "static" displacement technique. The relatively long mixing time of the stimulated-echo allows undesired dynamic components (shear waves and surface vibrations) to dampen such that static displacements are accurately encoded. Displacement phase shifts are measured relative to a reference file acquired with the object maintained in the same "State B". This obviates the need for image registration or feature tracking algorithms required by other static techniques. In fact, local displacement can be measured in a featureless continuum object. Moreover, the spatial resolution of displacement maps equals the resolution of the original image.

Despite these advantages, several parameters have yet to be optimized. In particular, a good balance between displacement sensitivity and NMR signal-to-noise (SNR) is required since optimization of one parameter may come at the expense of another. Computer simulations were performed to address these tradeoffs. Key parameters that affect SNR and displacement sensitivity include: displacement gradient amplitude and duration; applied deformation amplitude; image resolution; mixing time, TM; and tissue water diffusion properties. Figure 3 illustrates a simulation of applied displacement gradient amplitude and surface deformation (strain) on net SNR. As shown, a balance between phase (or, equivalently, displacement) sensitivity due to the applied surface deformation, the magnitude of the encoding gradient, and the signal loss due to diffusion must be obtained to maximize net SNR. If the combination of applied gradient and surface deformation is too small, no information about the tissue hardness will be obtained. If the combination is too large, intravoxel dephasing will lead to a loss of NMR signal, reducing the elasticity image SNR as well (the fall-off shown with increasing strain and gradient). Finally, a displacement encoding gradient that is too large will lead to diffusion losses, shown in Figure 3 as an overall attenuation as gradient is increased. Thus, these simulations suggest a net SNR gain via greater applied deformation with reduced gradient amplitude. (Previously, we acquired data at 4gauss/cm gradient strength and <0.02 surface strain which was well below the optimum settings). Mechanical reproducibility in the deformation device and patient tolerance are issues that need to be balanced against increasing the surface deformation. The deformation system is stable at 5mm surface deformations, which we anticipate will be well tolerated by patients.

Testing and implementation of the 3D displacement-encoding volume stimulated-echo sequence will begin once the mechanical deformation device is fully characterized at shorter mixing times. The spatial encoding segment of the pulse sequence (i.e., beyond the third rf-pulse) will be extended in an 8 – 16 echo train, fast-spin-echo (FSE) sequence. Slice axis phase encoding will be applied during the FSE echo train to yield the third spatial dimension of 8 – 16 slices. Addition of slice-direction displacement encoding is then straightforward.

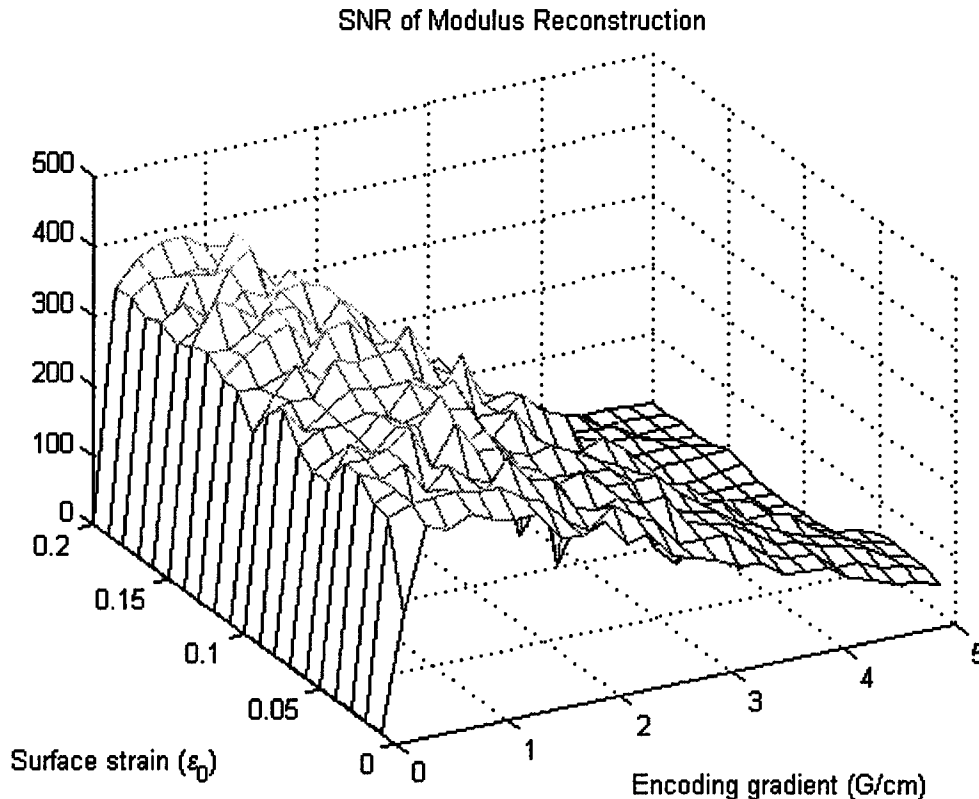


**Figure 3. Relative signal-to-noise as a function of applied deformation and displacement-encoding gradient strength.**

**Task 4: Month 1-12**

*Expansion of previously developed linear elasticity reconstruction algorithms for volumetric displacement and strain NMR measurements.*

The development and expansion of linear elasticity reconstruction algorithms were primarily focused on the following two aspects: a) development of boundary detection methods to identify the regions of uniform elasticity (Young's modulus) distribution, and b) development of volumetric linear elasticity reconstruction algorithms for optimized NMR displacement-encoded, volume simulated-echo pulse sequence.

**Boundary Detection.** The boundary detection is the first step in elasticity reconstruction, where strain images are processed to highlight boundaries between regions of different elastic modulus. Following boundary detection, closed contours of small elasticity variations are defined. The total dimension of the contour must include several resolution cells of the final reconstruction. The modulus along these contours can be considered constant, thereby providing a boundary condition for complete reconstruction of the elasticity within this region of interest (ROI) based on numerical solution of elasticity equations.

The boundary detection algorithm was developed for specifically NMR elasticity imaging. This algorithm is based on the stress continuity condition applicable for soft tissue deformations used in these studies.

For an inhomogeneous object, the boundary detection algorithm will give smoothly varying results everywhere except at the boundary points where elasticity changes. This is illustrated in Figure 4 where boundary detection was applied to the displacement and strain data from kidney-containing gel phantom. Three major regions of elastic inhomogeneity can be identified in Figure 4. Clearly, the gelatin background does not exhibit any changes in Young's modulus throughout the entire imaging plane. The kidney parenchyma appears as the most elastically different material in this phantom. Finally, the internal fatty tissue in the middle of the kidney is just slightly different from the gelatin.

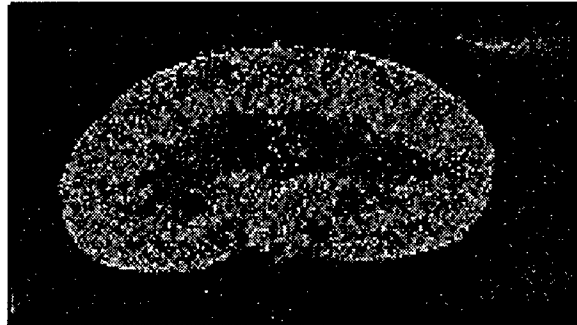


**Figure 4.** Boundary detection algorithm applied for gel-based phantom with embedded kidney. The longitudinal view of the kidney is depicted in this image, where kidney parenchyma and internal fatty regions are clearly identified.

In general, the approach presented in Figure 4 produces a qualitative reconstruction, i.e., boundary detection, and will require further more accurate Young's modulus reconstruction at every point of the volume or region of interest.

**Volumetric Linear Elasticity Reconstruction.** For a general, three-dimensional object, complete three-dimensional strain data are required. However, to reconstruct the Young's modulus in a single plane, all displacement components must only be measured in three closely positioned parallel planes intersecting the volume. From measurements in these three planes, coefficients needed for elasticity reconstruction in the central plane based on 3-D equilibrium equations can be calculated numerically with second order accuracy. Consequently, complete three-dimensional elasticity reconstruction can be done by moving the imaging planes in parallel. Note that even a pair of close parallel planes can also be used for numerical reconstruction in a single plane, but will, however, exhibit greater error since less accurate finite differences will be used to approximate all derivatives.

#### **Task 5: Month 10-26**

*Development of the nonlinear elasticity reconstruction model capable to process high-strain NMR images.*

The elasticity reconstruction problem can be posed in number of ways depending on the experimental conditions such as amount of surface deformations, type of phantom materials, etc. Previously, we have developed a reconstruction algorithm based on linear theory of elasticity, i.e., applicable for small deformations and linear elastic materials. However, both mechanical equilibrium equations and the displacement-strain relations must include high order spatial derivatives of the displacement if the average deformation is too large to be described with a linear model. An algorithm was developed to

reconstruct the elastic modulus of soft tissue for comparatively large surface deformations required for optimal SNR and sensitivity strain/displacement images. Numerical methods were developed to reduce error propagation in reconstruction algorithms.

### **Technical Objective II: Phantom Studies on 2T 18cm Bore MRI System**

#### **Task 6: Month 7-22**

*Development of gel- and rubber-based phantoms with tissue mimicking elastic and NMR relaxation properties. Time-stable phantoms with non-palpable inclusions of various shapes and elasticity contrast positioned at different locations within the phantom will be produced.*

During the first year of the project, we have identified and carefully tested the materials for tissue mimicking phantoms. Our ultimate goal is to simulate the anatomical and geometrical features of the normal and pathologically transformed breast using these materials. The models of breast containing single or multiple inclusions are presented in Figure 5. These models were fabricated using plastisol material (M-F Manufacturing Co., Fort Worth, Texas, USA).

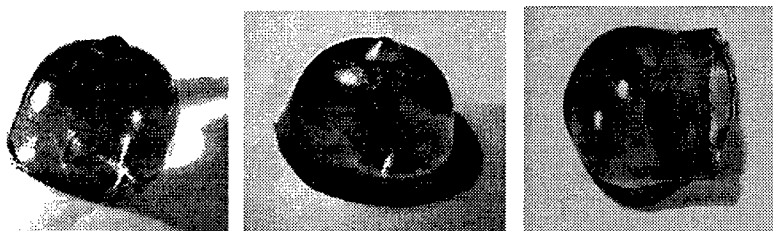


**Figure 5. Plastisol based models of breast with various inclusions.**

Our recent studies, however, suggested that silicone gels (Semicosil 921, Wacker Silicones Co., Adrian, Michigan, USA) could better simulate the mechanical and NMR relaxation properties of the tissue. Initial silicone gel based homogeneous phantoms were produced for mechanical and NMR testing.

**The following Technical Objectives and Tasks will be addressed in Years 2 and 3 of the project, but are listed below for completeness.**

#### **Task 7: Month 12-26**

*Investigation of the capabilities of 3-D NMR elasticity imaging, i.e., determine sensitivity, accuracy and resolution of NMR displacement and strain images, and reconstructed elasticity (Young's modulus) distribution.*

### **Technical Objective III: Translation to 1.5T Human MRI System**

#### **Task 8: Month 20-25**

*Design and construction of the compression device compatible with human breast NMR imaging system and capable to produce wide range of surface deformations. Development of sophisticated circuits to control surface deformations and time synchronization with human MRI system.*

**Task 9: Month 24-34**

*Development of appropriate for clinical studies 3-D displacement encoded, volume stimulated-echo pulse sequence on human MRI system with data acquisition time within or comparable to regular MRI examination.*

**Task 10: Month 22-34**

*Development of time efficient elasticity reconstruction algorithms more suitable for clinical applications.*

**Task 11: Month 20-30**

*Estimate the influence of the cardiac and respiratory motion to elasticity images and develop the approaches to reduce these artifacts.*

**Task 12: Month 30-36**

*Validation of clinical NMR data acquisition and elasticity reconstruction methods on breast tissue mimicking phantoms.*

## **CONCLUSIONS**

Design, fabrication, and refinement of the deformation device essential for phantom studies required more time than originally planned. The current version of deformation system, however, meets the requirements to deliver highly reproducible surface deformations of the imaged object. A dedicated TTL control circuit was developed to adjust delay and duration of pulses that drive pneumatic relays in synchrony with in imaging sequence. The complete MRI-compatible hardware, pneumatic components, and control circuitry are now fully operational. Pulse sequence refinements were investigated via simulations that indicate we were previously operating at a sub-optimal regime. We have adjusted our acquisition procedures accordingly, and will soon embark on 3D spatial / 3D displacement encoding phantom experiments. Good progress has been made to refine 3D elasticity reconstruction and edge detection algorithms, although require additional phantom data is required to further test these strategies. The first of these data will be collected in the next few months.

Significant effort was directed to develop suitable phantom materials. Requirements include: temporally stable (over months-years); adjustable mechanical properties to match a range of tissues; moldable to simple geometries; tissue-like NMR properties. The Semocsil 921 silicone gel generally meets these requirements (with the exception of tissue-like diffusion) and will be used in subsequent phantom studies.

## References

1. A. P. Sarvazyan, A. R. Skovoroda, S. Y. Emelianov, J. B. Fowlkes, J. G. Pipe, R. S. Adler, R. B. Buxton, P. L. Carson, "Biophysical Bases of Elasticity Imaging. Acoustical Imaging," 21, Plenum Press, New York, p. 223-240, 1995.
2. A. R. Skovoroda, A. N. Klishko, D. A. Gukasyan, E. I. Maevsky, V. D. Ermilova, G. A. Oranskaya, and A. P. Sarvazyan, Quantitative analysis of the mechanical characteristics of pathologically altered soft biological tissues. *Biofizika*, 40(6), 1335-1340, (1995).
3. D. Hill, V. White, D. Jolley, Mapperson, Self examination of the breast: is it beneficial? Meta-analysis of studies investigating breast self examination and the extent of disease in patients with breast cancer. *Br J Med* 297, 271-275 (1988).
4. P. A. Newcomb, S. Weiss, B. E. Storer, D. Scholes, B. E. Young, Breast self examination in relation to the occurrence of advanced breast cancer. *J Natl Cancer Inst* 83, 260-265 (1991).
5. R. J. Dickinson, C. R. Hill, Measurement of soft tissue motion using correlation between A-scans. *Ultrasound Med Biol* 8, 263-271 (1982).
6. M. Tristam, D. C. Barbosa, D. O. Cosgrove, D. K. Nassiri, J. C. Bamber, C. R. Hill, Ultrasonic study of in vivo kinetic characteristics of human tissue. *Ultrasound Med Biol* 12, 927-937 (1986).
7. M. Tristam, D. C. Barbosa, D. O. Cosgrove, J. C. Bamber, C. R. Hill, Application of Fourier analysis to clinical study of patterns of tissue movement. *Ultrasound Med Biol* 14, 695-707 (1988).
8. R. M. Lerner, S. R. Huang, K. J. Parker, "Sono-elasticity" images derived from ultrasound signals in mechanically vibrated tissues. *Ultrasound Med Biol* 16, 231-239 (1990).
9. K. J. Parker, S. R. Huang, R. A. Musulin, R. M. Lerner, Tissue response to mechanical vibrations for "sonoelasticity imaging". *Ultrasound Med Biol* 16, 241-246 (1990).
10. K. J. Parker, R. M. Lerner, Sonoelasticity of organs: shear waves ring a bell. *J Ultrasound Med* 11, 387-392 (1992).
11. J. Ophir, I. Cespedes, H. Ponnekanti, Y. Yazdi, X. Li, Elastography: a quantitative method for imaging the elasticity of biological tissues. *Ultrason Imaging* 13, 111-134 (1991).
12. B. S. Garra, E. I. Cespedes, J. Ophir, S. R. Spratt, R. A. Zuurbier, C. M. Magnant, M. F. Pennanen, Elastography of breast lesions: initial clinical results. *Radiology* 202, 79-86 (1997).

13. M. O'Donnell, A. R. Skovoroda, B. M. Shapo, S. Y. Emelianov, Internal displacement and strain imaging using ultrasonic speckle tracking. *IEEE Transactions on Ultrasonic Ferroelectrics and Frequency Control* 41, 314-325 (1994).
14. S. Y. Emelianov, M. A. Lubinski, W. F. Weitzel, R. C. Wiggins, A. R. Skovoroda, M. O'Donnell, Elasticity imaging for early detection of renal pathologies. *Ultrasound Med Biol* 21 (7), 871-883, (1995).
15. L. Axel, L. Dougherty, Heart wall motion: improved method of spatial modulation of magnetization for MR imaging. *Radiology* 169, 59-63 (1988).
16. E. A. Zerhouni, D. M. Parish, W. J. Rogers, A. Yang, E. P. Shapiro, Human heart: tagging with MR imaging - a method for noninvasive assessment of myocardial motion. *Radiology* 169, 164-172 (1988).
17. N. J. Pelc, M. Drangova, L. R. Pelc, Y. Zhu, D. C. Noll, B. S. Bowman, R. J. Herfkens, Tracking of cyclic motion with phase-contrast cine MR velocity data *J Magn Reson Imaging*, 5(3), 339-345 (1995).
18. J. B. Fowlkes, S. Y. Emelianov, J. G. Pipe, A. R. Skovoroda, R. S. Adler, P. L. Carson, A. P. Sarvazyan, Magnetic resonance imaging techniques for detection of elasticity variation. *Med Phys* 22(11) 1771-1778, (1995).
19. R. Muthupillai, D. J. Lomas, P. J. Rossman, J. F. Greenleaf, A. Manduca, R. L. Ehman, Magnetic resonance elastography by direct visualization of propagating acoustic strain waves. *Science* 269, 1854-1857 (1995).
20. R. Muthupillai, P. J. Rossman, J. F. Greenleaf, S. J. Riederer, R. L. Ehman, MR imaging of acoustic strain waves: initial in vivo results, in "Proc., International Society for Magnetic Resonance in Medicine, 1996," p. 475.
21. D. B. Plewes, I. Betty, S. N. Urchuk, I. Soutar, Visualizing Tissue Compliance with MR Imaging. *J Magn Reson Imaging* 5, 733-738 (1995).
22. D. B. Plewes, G. Poole, M. Leitch, S. N. Urchuk, MR assessment of the viscoelastic properties of tissue through the propagation of transient strain waves, in "Proc., International Society for Magnetic Resonance in Medicine, 1996," p. 476.
23. I. Cespedes, J. Ophir, H. Ponnekanti, N. Maklad, Elastography: elasticity imaging using ultrasound with application to muscle and breast in vivo. *Ultrason Imaging* 15, 73-88 (1993).
24. A. Skovoroda, S. Emelianov, M. Lubinski, A. Sarvazyan, M. O'Donnell, Theoretical analysis and verification of ultrasound displacement and strain imaging.

IEEE Transactions on Ultrasonic Ferroelectrics and Frequency Control 41(3), 302-313 (1994).

25. A. Skovoroda, S. Emelianov, M. O'Donnell, Tissue elasticity reconstruction based on ultrasound displacement and strain images: IEEE Transactions on Ultrasonic Ferroelectrics and Frequency Control, 42(4), pp. 747-765 (1995).
26. S. Y. Emelianov, A. R. Skovoroda, M. A. Lubinski, M. O'Donnell, Reconstructive elasticity imaging. Acoustical Imaging, " 21, Plenum Press, New York, p. 241-253, 1995.
27. T.L. Chenevert, S.Y. Emelianov, A.R. Skovoroda: Elasticity Reconstructive Imaging Using Static Displacement and Strain Estimations. Proceedings of the International Society of Magnetic Resonance in Medicine, p-461, 1997.
28. T.L. Chenevert, A.R. Skovoroda, M. O'Donnell, and S.Y. Emelianov, "Elasticity reconstructive imaging via stimulated echo MRI," Magnetic Resonance in Medicine, 39, pp. 482-490 (1998). See Appendix.

## APPENDIX

Reprint of: "Elasticity reconstructive imaging via stimulated echo MRI," T.L. Chenevert, A.R. Skovoroda, M. O'Donnell, and S.Y. Emelianov, Magnetic Resonance in Medicine, 39, pp. 482-490 (1998)

# Elasticity Reconstructive Imaging by Means of Stimulated Echo MRI

Thomas L. Chenevert, Andrei R. Skovoroda, Matthew O'Donnell, Stanislav Y. Emelianov

A method is introduced to measure internal mechanical displacement and strain by means of MRI. Such measurements are needed to reconstruct an image of the elastic Young's modulus. A stimulated echo acquisition sequence with additional gradient pulses encodes internal displacements in response to an externally applied differential deformation. The sequence provides an accurate measure of static displacement by limiting the mechanical transitions to the mixing period of the simulated echo. Elasticity reconstruction involves definition of a region of interest having uniform Young's modulus along its boundary and subsequent solution of the discretized elasticity equilibrium equations. Data acquisition and reconstruction were performed on a urethane rubber phantom of known elastic properties and an *ex vivo* canine kidney phantom using <2% differential deformation. Regional elastic properties are well represented on Young's modulus images. The long-term objective of this work is to provide a means for remote palpation and elasticity quantitation in deep tissues otherwise inaccessible to manual palpation.

**Key words:** elastic Young's modulus; magnetic resonance imaging; elastography; strain imaging.

## INTRODUCTION

It is well known that tissue elastic properties may be altered by tumors. Young's elastic moduli may differ by orders of magnitude in soft tissues in various physiologic states (1, 2). This finding is the physical basis behind manual palpation used to detect "hard" masses (3, 4). Indeed, physical examination is the first diagnostic line of defense against breast cancer, because nodule hardness raises suspicion of malignancy. Detection of a new breast mass by physical examination is often sufficient for surgical excisional biopsy, even when not corroborated by other diagnostic tests. Manual palpation of the prostate, superficial lymph nodes, and abdominal organs are also commonly performed. Unfortunately, sensitivity of palpation is relatively poor within deep, dense, or heterogeneous tissues. Although the touch of a skilled interpreter is considered a powerful diagnostic instrument, most lesions detected by palpation tend to be relatively large and superficial.

### MRM 39:482-490 (1998)

From the Departments of Radiology (T.L.C.), Biomedical Engineering (S.Y.E.), and Electrical Engineering & Computer Science (M.O.), University of Michigan, Ann Arbor, Michigan; and Institute of Mathematical Problems of Biology (A.R.S., S.Y.E.), Russian Academy of Sciences, Pushchino, Russia.

Address correspondence to: Dr. Thomas L. Chenevert, University of Michigan Hospitals, Department of Radiology - MRI, 1500 E. Medical Center Drive, Ann Arbor, MI 48109-0030.

This research was supported in part by the National Institutes of Health grant DK47324 and by US Army grant DAMD17-97-7079.

Received April 15, 1997; revised September 8, 1997; accepted September 9, 1997.

Scientists are attempting to electronically extend the touch of the physical examiner using a variety of image-based techniques that infer tissue elasticity. The essential element is measurement of internal motion and strain in tissue structures experiencing mechanical stress. To date, most "elastography" has used ultrasound to track the relative motion of targets by specular reflection (5-7), by Doppler techniques (8-10), by cross-correlation of raw or processed acoustic echoes (11, 12), or by tracking speckle patterns (13-15). Usually an external static or dynamic deformation is applied while internal displacements or propagating shear waves are documented by imaging.

MRI has also been used to measure internal displacement and strain components of the heart using spatial magnetization tagging (16, 17) and phase-based velocity encoding (18). Elasticity reconstruction of an externally deformed phantom was demonstrated using magnetization tagging, but this method has spatial resolution limited by the tagged grid size and only measures 2D motion (19). More recently, motion phase encoding by means of bipolar gradients was used to produce two-dimensional (2D) displacement and strain maps in media mechanically driven by external forces (20-23). Strain and displacement maps infer internal elasticity but are also strongly affected by the applied deformational geometry. Consequently, these maps do not uniquely reflect internal tissue properties (i.e., elastic Young's modulus). Maps of dynamic strain-wave propagation, however, do allow measurement of local strain wavelength or velocity from which the local elastic modulus can be derived (20). Shear-wave attenuation, interference from standing waves off multiple reflectors, and limited resolvable points over the shear wavelength are potential drawbacks of this approach.

Relative to ultrasound, MRI has an advantage in overall resolution and accuracy for multidimensional displacement and strain measurement needed for elasticity reconstruction. Ultrasound can accurately measure axial (i.e., along the beam axis) motion at high spatial resolution ( $\leq$  millimeter), but lateral displacement is measured at much lower spatial resolution defined by the depth-dependent acoustic beam width. The third dimension is generally not even considered given the limitations of ultrasound. Consequently, reduced motion dimensionality and overall low motion resolution of the imaging system compromise the "elastogram." This shortcoming, in turn, constrains the mechanical model used in elasticity reconstruction. To date, only 1D motion models have been applied to ultrasound-derived elasticity images of tissues *in vivo* (12, 24). More accurate elasticity images are achieved by properly controlling external deformation.

tions, leading to 2D elasticity reconstruction within the imaging plane (25, 26).

In this work we present a method to spatially encode internal displacement of an object that has undergone an externally applied "static" deformation with subsequent reconstruction into elasticity maps. Unlike dynamic techniques designed to estimate elasticity from observations related to strain-wave propagation, static elasticity reconstruction involves estimation of local strain from displacement and numerical solution of differential elasticity equilibrium equations.

## THEORY OF RECONSTRUCTIVE ELASTICITY IMAGING

The goal of elasticity imaging is to reconstruct the elastic modulus of a desired tissue region using available measurements of displacement and strain components. Indeed, the mechanical properties of tissue are ultimately linked to the patterns of internal deformations, but the deformational geometry can greatly affect these patterns as well. To uniquely image tissue elasticity, the Young's modulus must be reconstructed from estimates of internal displacement and strain.

In this paper, the general approach to elasticity reconstruction was based on a model of linear, elastic, isotropic, incompressible media (26, 27). The key equations and considerations are briefly presented here. A more detailed description of elasticity reconstruction is given in an earlier publication (26).

In linear elasticity, the components of the strain ( $\varepsilon_{ij}$ ) and stress ( $\sigma_{ij}$ ) tensors under static deformation are:

$$\varepsilon_{ij} = \frac{1}{2} \left( \frac{\partial u_i}{\partial x_j} + \frac{\partial u_j}{\partial x_i} \right) = \frac{1}{2} (u_{i,j} + u_{j,i}) \quad [1]$$

$$\sigma_{ij} = p\delta_{ij} + \frac{2}{3} E\varepsilon_{ij} \quad [2]$$

where  $u_i$  is a component of the displacement vector  $\mathbf{U} = (u_1, u_2, u_3)$  in Cartesian coordinates  $\mathbf{X} = (x_1, x_2, x_3)$ ,  $p$  is the static internal pressure,  $\delta_{ij}$  is the Kronecker delta symbol, and  $E = E(x_1, x_2, x_3)$  is the Young's elastic modulus. Note in Eq. [1], and the entire paper, the lower index after a comma means differentiation with respect to the corresponding spatial coordinate.

The static deformation of the medium can be described by the equilibrium condition:

$$\sum_{j=1}^3 \sigma_{ij,j} + f_i = 0, \quad i = 1, 2, 3 \quad [3]$$

where  $f_i$  is the body force per unit volume acting in the  $x_i$  direction. In addition, volume conservation for an incompressible medium leads to the following relationship between displacement and strain components

$$\nabla \cdot \mathbf{U} = \varepsilon_{11} + \varepsilon_{22} + \varepsilon_{33} = u_{1,1} + u_{2,2} + u_{3,3} = 0 \quad [4]$$

Using Eqs. [1] and [2] for stress and strain components, and the incompressibility Eq. [4], the equilibrium condi-

tion with eliminated internal pressure  $p$  can be rewritten in the following form:

$$\begin{aligned} & 2\varepsilon_{12}(E_{,11} - E_{,22}) + 2(u_{2,2} - u_{1,1})E_{,12} + 2\varepsilon_{23}E_{,13} \\ & - 2\varepsilon_{13}E_{,23} + (\nabla^2 u_2 + \omega_{12,1})E_{,1} - (\nabla^2 u_1 - \omega_{12,2})E_{,2} \\ & + \omega_{12,3}E_{,3} + \nabla^2 \omega_{12}E + 3(f_{2,1} - f_{1,2}) = 0 \\ & 2\varepsilon_{13}(E_{,11} - E_{,33}) + 2\varepsilon_{23}E_{,12} + 2(u_{3,3} - u_{1,1})E_{,13} \\ & - 2\varepsilon_{12}E_{,23} + (\nabla^2 u_3 + \omega_{13,1})E_{,1} + \omega_{13,2}E_{,2} \\ & - (\nabla^2 u_1 - \omega_{13,3})E_{,3} + \nabla^2 \omega_{13}E + 3(f_{3,1} - f_{1,3}) = 0 \end{aligned} \quad [5]$$

$$\begin{aligned} & 2\varepsilon_{23}(E_{,22} - E_{,33}) + 2\varepsilon_{13}E_{,12} - 2\varepsilon_{12}E_{,13} + 2(u_{3,3} \\ & - u_{2,2})E_{,23} + \omega_{23,1}E_{,1} + (\nabla^2 u_3 + \omega_{23,2})E_{,2} - (\nabla^2 u_2 \\ & - \omega_{23,3})E_{,3} + \nabla^2 \omega_{23}E + 3(f_{3,2} - f_{2,3}) = 0 \end{aligned}$$

$$\omega_{12} = u_{2,1} - u_{1,2}, \quad \omega_{13} = u_{3,1} - u_{1,3}, \quad \omega_{23} = u_{3,2} - u_{2,3}$$

Clearly, the elasticity reconstruction process based on Eq. [5] requires accurate measurements of the displacement vector, or, to be more precise, requires accurate estimation of up to third-order spatial derivatives of the displacement. Equation [5] can also be written in terms of spatial derivatives of strain tensor components. The unique solution of the system of coupled partial differential equations [5] is determined by the boundary conditions, i.e., the elastic modulus  $E(\mathbf{X})$  must be given along the boundary of the reconstruction region of interest (ROI). It should also be noted here that the analytical solution of Eq. [5] is not generally possible, and numerical methods must be developed to solve this system of partial differential equations.

Based on the particular geometry of the phantoms and deformation system used in these experiments, Eq. [5] was simplified. A 2D approximation of Eq. [5] was used because the imaged plane was near the center of the

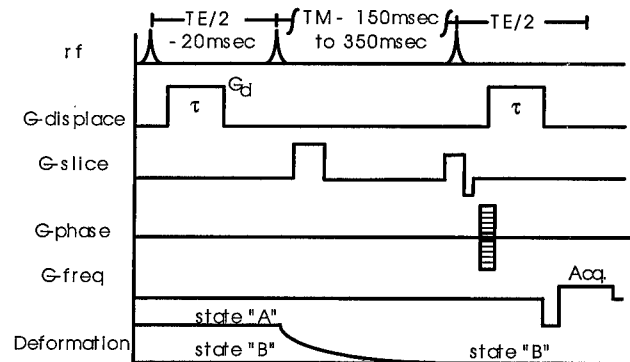


FIG. 1. Stimulated-echo data acquisition and object deformation sequence. Mechanical transitions occur during the long mixing time (TM) such that a static displacement equilibrium is achieved. Local displacement between deformation states "A" and "B" are encoded by phase shift proportional to "G-displace" amplitude  $G_d$ , and duration  $\tau$ .

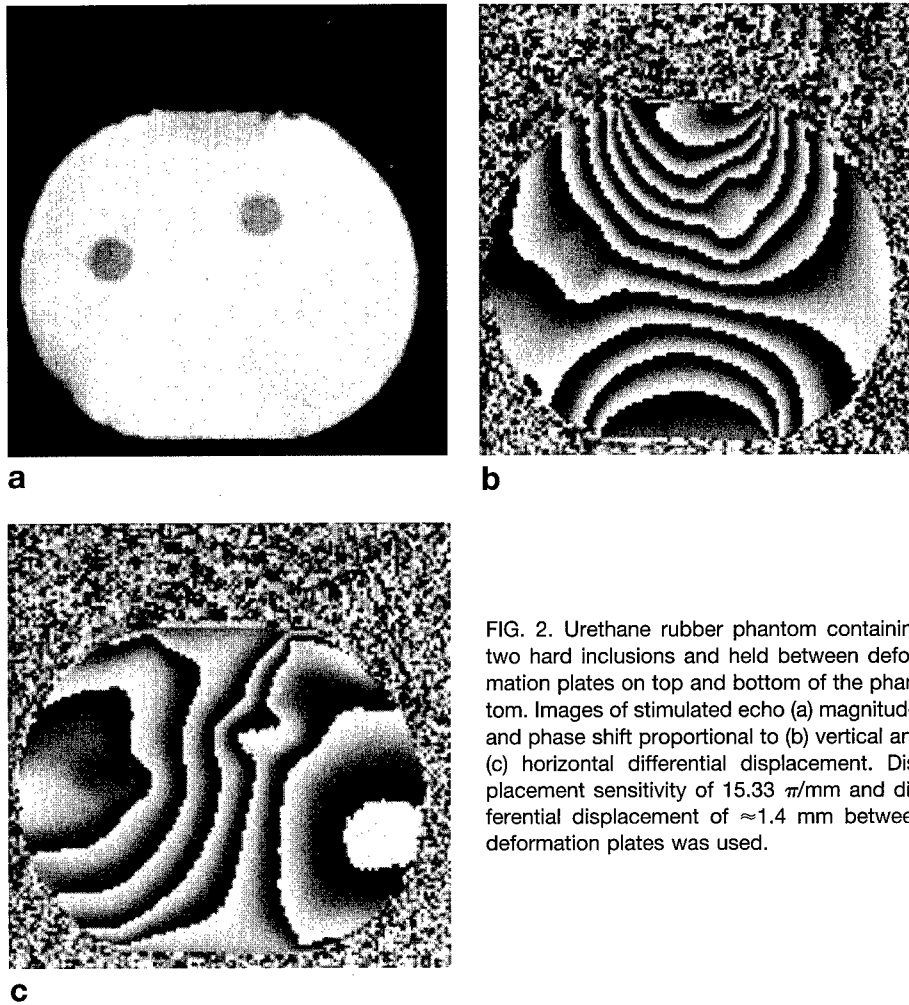


FIG. 2. Urethane rubber phantom containing two hard inclusions and held between deformation plates on top and bottom of the phantom. Images of stimulated echo (a) magnitude, and phase shift proportional to (b) vertical and (c) horizontal differential displacement. Displacement sensitivity of  $15.33 \pi/\text{mm}$  and differential displacement of  $\approx 1.4 \text{ mm}$  between deformation plates was used.

phantom. For such a plane (arbitrarily denoted as  $x_3 = 0$ ), the displacement vector components do not vary significantly as a function of the out-of-plane  $x_3$  coordinate, and therefore, the “plane strain state” condition is applicable. With this condition, Eq. [5] reduces to a single nontrivial equation:

$$\begin{aligned} & (E_{11} - E_{22})(u_{1,2} + u_{2,1}) + 2E_{12}(u_{2,2} - u_{1,1}) \\ & + 2E_{,1}(u_{2,11} + u_{2,22}) - 2E_{,2}(u_{1,11} + u_{1,22}) \\ & + E(u_{2,111} + u_{2,221} - u_{1,112} - u_{1,222}) + 3(f_{2,1} - f_{1,2}) = 0 \end{aligned} \quad [6]$$

Under conditions in which these assumptions are valid, only in-plane displacement  $u_1$  and  $u_2$  or their derivatives are needed to reconstruct the modulus in the plane  $x_3 = 0$ .

#### Static Displacement Measurement by Means of Stimulated Echo MRI

Shear-wave propagation speed in soft tissue is 1–20 m/s. Consequently, a shear wave imparted by a single-stroke or an oscillating deformation force may require tens of milliseconds to traverse an object  $\approx 100 \text{ mm}$  in size. The time for reflected waves to dampen may be much longer. “Dynamic” measurements, which encode displacement during shear-wave propagation, are potentially con-

founded by interference of the primary shear wave with reflected or standing shear waves. To avoid this condition, a “static” displacement encoding approach was adopted. It requires measurement of internal displacement between two or multiple deformations while the object is in mechanical equilibrium for each measurement. A stimulated echo sequence with displacement-encoding gradient pulses is used to achieve this, as shown in Fig. 1. Mechanical transition from state “A” to state “B” occurs during the stimulated echo mixing time,  $T_M$ . A relatively long mixing time allows long-lived elastic vibrations to dampen before spatial encoding. Because the relevant magnetization during  $T_M$  is longitudinal, it is unaffected by potentially ill-defined motions during the mechanical transition period. As a result, a more accurate static deformation measurement is achieved. Also note that precise synchronization of mechanical and pulsed gradient events is not critical as long as the mechanical transition begins after the second RF pulse

and is complete before the third RF pulse. Similarly, a long delay in  $TE$  could be used, but this is done at the expense of signal lost to  $T_2$  decay.

Local displacement is encoded by means of phase shift governed by pulsed-field gradient factors,

$$\Phi_d = \gamma \vec{G}_d \tau \quad [7]$$

where displacement sensitivity,  $\Phi_d$ , is in units of (radians/distance). A phase reference acquisition is required for each displacement encode condition to remove pre-existing phase shifts that are unrelated to displacement. Reference data are acquired using the same pulse sequence, including displacement encode gradient pulses, but with the object maintained in state B. Note that all spatial encoding occurs from the third RF pulse and beyond. That is, the object is in one deformation state (state B) for both displacement and phase reference acquisitions during all spatial encoding segments of the sequence. Consequently, image registration or feature tracking algorithms (14) are not required to estimate displacement. Instead, local displacement is encoded directly by local phase of a corrected dataset,  $S_{cor}$ , given by,

$$S_{cor}(\vec{r}) = \frac{S_A(\vec{r}) S_B(\vec{r})^*}{|S_B(\vec{r})|} \cong |S_A(\vec{r})| e^{i\varphi(\vec{r})} \quad [8]$$

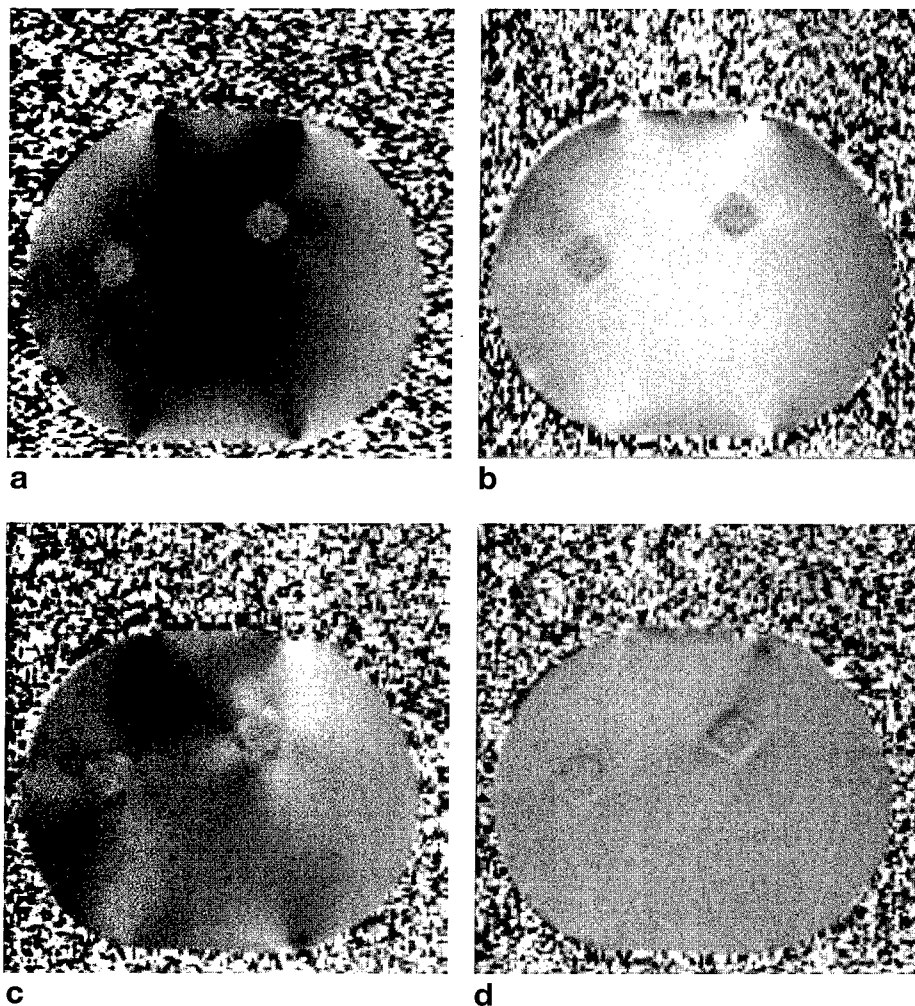


FIG. 3. Strain images calculated from first-order derivatives of the displacement images represented in Fig. 2. Normal strains (a)  $\epsilon_{11}$  and (b)  $\epsilon_{22}$ , and (c) shear strain  $\epsilon_{12} = \epsilon_{21}$  reflect internal elastic properties and the externally applied deformation field. The plane strain state assumption and phantom incompressibility suggest  $\epsilon_{11} \approx -\epsilon_{22}$  as is supported by the relatively featureless map of  $\epsilon_{11} + \epsilon_{22}$  in (d).

where  $S_A$  and  $S_B$  are the data acquired with the object initially in state A and state B, respectively. The unwrapped phase of the corrected dataset and Eq. [7] provides a local measure of displacement,  $U$ , by means of;

$$\varphi(\vec{r}) = \vec{\Phi}_d \cdot [\vec{r}_A - \vec{r}_B] = \vec{\Phi}_d \cdot U(\vec{r}) \quad [9]$$

Most sources of phase error, such as static field inhomogeneity, tend to be slowly varying functions of position. Therefore, the phase reference datasets may be acquired at relatively low spatial resolution to reduce scan time.

## METHODS

### Data Acquisition

Elasticity imaging was performed on two phantoms. One was an 85-mm diameter cylindrical urethane rubber phantom containing two 8-mm cylinders of hard material. Previously, the ratio of Young's modulus between the inclusion and background material was measured

$10.5 \pm 1.5$  for 30% surface deformation (19). In the present study, smaller surface deformation was applied, and consequently, the elasticity contrast within this phantom should be less than the previously measured ratio. Whereas the mechanical properties of the rubber phantom mimic soft tissue, the phantom had inherently poor NMR signal. A more tissue-equivalent phantom in terms of NMR and mechanical properties was achieved by embedding a fresh canine dog kidney (<24 h *ex vivo*) into a 130 mm  $\times$  105 mm  $\times$  75 mm block of 5% gelatin. One hour before MRI, 10 ml of 5% glutaraldehyde solution was injected into kidney parenchyma to create a hard lesion(s).

Phantoms were held securely in place under moderate preload pressure by two parallel acrylic plates. When pressure to the top plate was released, the phantom recoiled vertically an amount constrained by physical stops. Maximum vertical displacement was <1.5 mm, which represented <2% differential between state "A" (greater deformation) and state "B" (less deformation). Deformation was actuated pneumatically by an air-filled bladder on top of the phantom holder. Pneumatic pressure was stepped by a remote solenoid valve with timing controlled by an external transistor transistor logic (TTL) gate circuit triggered by the pulse sequence.

Displacement encoding gradient pulse duration,  $\tau = 4.5$  msec, and amplitude,  $G_d = 40$  mT/m, provided a displacement sensitivity of  $\Phi_d = 15.33 \pi/\text{mm}$  by means of Eq. [7]. The displacement encoding direction was alternated each pulse repetition between vertical and horizontal. For the urethane rubber phantom, acquisition parameters were  $TR = 1.3$  s,  $TM = 350$  msec,  $TE = 50$  msec,  $128 \times 128$  matrix, four signal averages, 100 mm field of view, and 10-mm section thickness. An additional  $128 \times 32$  matrix acquisition was collected for phase-reference correction of vertical and horizontal encoded data. The kidney phantom acquisition parameters were  $TR = 1$  s,  $TM = 200$  msec,  $TE = 76$  msec,  $256 \times 256$  matrix, two signal averages, 150 mm field of view, and 5-mm section thickness; with a  $256 \times 32$  dataset acquired for phase correction. All experiments were performed on a 2 T 18-cm bore MRI system (Bruker, formerly GE NMR

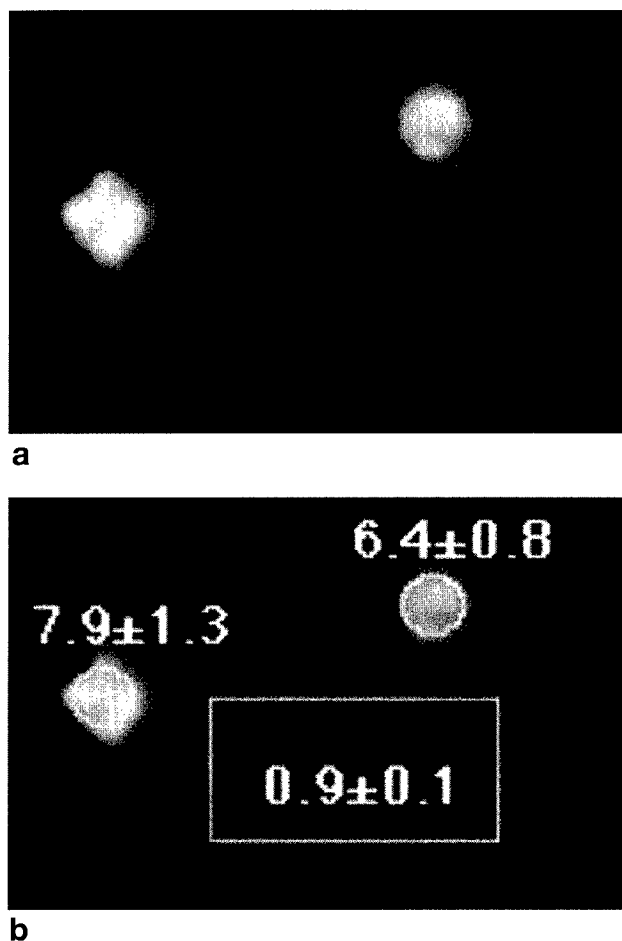


FIG. 4. (a) Reconstructed map of Young's modulus for the urethane rubber phantom within a  $63 \times 50$  mm region. The boundary of the region is defined to have a Young's modulus = 1. Relative Young's moduli for inclusions and background material are shown in (b).

Instruments), using a 150-mm transmit/receive birdcage coil.

#### Data Processing

Time-domain data were transferred for off-line processing as follows. Phase reference datasets were zero-filled and 2D Fourier transformed to a  $128 \times 128$  or  $256 \times 256$  matrix for phase correction by means of Eq. [7]. The resulting phase maps were used to estimate the spatial derivatives of the in-plane displacements necessary for elasticity reconstruction (6). Note phase unwrapping is not strictly required because only phase derivatives are used. Assuming the displacement fields are continuous, resulting in small differential displacement at any pixel compared with the total displacement, the differential displacement between two neighboring pixels was directly computed from the angle of the complex multiplication of each pixel with the conjugate of the neighboring pixel, then scaled by  $1/\Phi_d$ .

Solving Eq. [6] for unknown  $E(x_1, x_2)$  performed the elasticity reconstruction, i.e., reconstruction of the spatial distribution of elastic Young's modulus. As was noted previously, the unique solution of a boundary value problem (Eq. [5] or [6]) is determined by the bound-

ary conditions. Therefore, a rectangular ROI was identified within the imaging planes for both phantoms. For the phantom with two hard inclusions, the ROI was a region of  $63 \times 50$  mm positioned approximately in the center of the phantom and included both inclusions. For the canine kidney phantom, the rectangular  $94 \times 51$  mm ROI included the whole kidney cross-section. In both cases, the Young's modulus value along the ROI boundary was set to "one" resulting in reconstruction of relative Young's modulus. More detailed analysis and discussion of defining the ROI was considered previously (26).

Elasticity reconstruction Eqs. [5] and [6] assume that spatial derivatives of the Young's modulus are continuous functions. To ensure continuous elasticity distribution, the spatial derivatives of the displacement were low-pass filtered before elasticity reconstruction, resulting in mild spatial resolution reduction.

After defining the boundary conditions, Eq. [6] was discretized over the ROI with the same grid spacing as the MR images, where all spatial derivatives of the displacement/strain (i.e., coefficients in Eq. [6] for unknown Young's modulus distribution) were approximated by finite differences. The linear set of equations resulting from discretization of Eq. [6] was solved iteratively, where the error in each step was estimated by averaging the left-hand side of Eq. [6] over the ROI using the current estimate of the elasticity distribution. From step to step, the Young's modulus distribution was updated based on the changes in the average error.

#### RESULTS

Magnitude and corrected phase images of the urethane rubber phantom are shown in Fig. 2. Given that  $\Phi_d = 15.33 \pi/\text{mm}$ , the number of  $2\pi$  phase bands in Fig. 2b indicates that the vertical excursion of the phantom top relative to the bottom was  $\approx 1.4$  mm; similarly, the relative lateral displacement between left and right edges of the phantom was  $\approx 0.8$  mm (Fig. 2c). Reduced phase slopes in the regions of the hard inclusions are clearly visible on the phase images. Normal strain,  $\epsilon_{11}$  and  $\epsilon_{22}$ , and shear strain,  $\epsilon_{12} = \epsilon_{21}$ , maps are illustrated in Figs. 3a–3c, respectively. The observed contrast reversal between  $\epsilon_{11}$  and  $\epsilon_{22}$  is a result of phantom incompressibility (like soft tissue), which yields  $\epsilon_{11} = -\epsilon_{22}$  assuming negligible out-of-plane strain. Consequently, the sum ( $\epsilon_{11} + \epsilon_{22}$ ) is relatively "flat" as shown at equivalent grayscale settings in Fig. 3d. Also note, whereas the strain maps clearly exhibit object-specific detail (i.e., inclusions), features related to the applied external deformation are quite conspicuous. This fact demonstrates why an elasticity reconstruction is needed. The Young's modulus was reconstructed for a  $63 \times 50$  mm region as presented in Fig. 4a. The boundary of the elasticity reconstruction area was defined to have value "1." The relative elastic moduli for select regions are indicated in Fig. 4b and are consistent with the known elasticity of these materials (19).

The canine kidney phantom is shown in Fig. 5 as magnitude (Fig. 5a), vertical (Fig. 5b), and horizontal (Fig. 5c) phase shift images. It is apparent from the vertical phase image (Fig. 5b) that although  $\approx 1.24$ -mm rel-

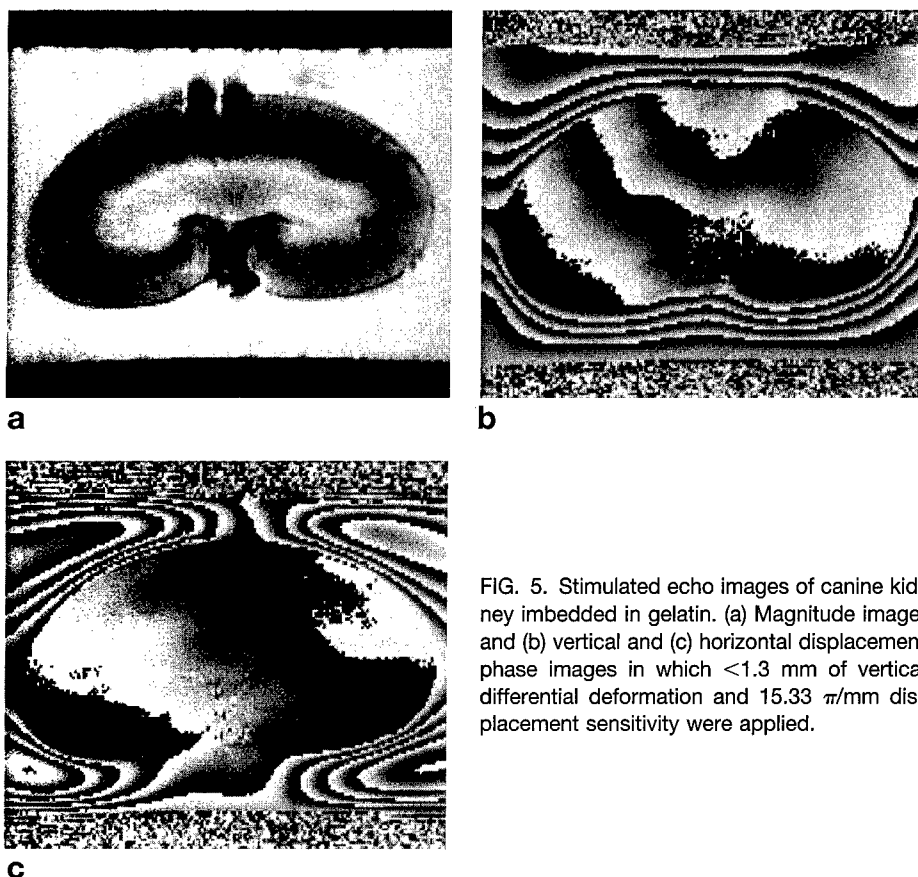


FIG. 5. Stimulated echo images of canine kidney imbedded in gelatin. (a) Magnitude image, and (b) vertical and (c) horizontal displacement phase images in which  $<1.3$  mm of vertical differential deformation and  $15.33 \pi/\text{mm}$  displacement sensitivity were applied.

active displacement spans the full phantom, only  $\approx 0.26$  mm of it is within the kidney. Consequently, there is a high concentration of strain near the gel-kidney interface, as is clear on the strain maps (Fig. 6). As noted before, strain images exhibit contrast related to a combination of internal structure and the externally applied deformation. Elasticity reconstruction, however, reduces the ambiguity and exhibits contrast dominated by internal elastic properties (Fig. 7a). It is also encouraging to note that whereas there was only moderate strain contrast within the kidney, elasticity contrast within renal parenchyma and central sinus are well distinguished on the Young's modulus image. Moreover, the site of glutaraldehyde injection (top-right quadrant of images) exhibited the highest relative Young's modulus. Approximately 20 h after MRI, the kidney phantom was sliced at a plane corresponding to that studied by MRI. An optical image of this slice is shown in Fig. 7c. The freshly cut surface was palpated such that areas of relatively "hard" parenchyma could be noted. Arrows in Fig. 7c mark the most conspicuous areas of hardness; the largest area corresponds to the high Young's modulus region in the upper-right quadrant of the kidney.

## DISCUSSION

In this work we introduce a method to image and quantify internal elastic properties of an object by means of displacement-sensitive MRI with associated elasticity reconstruction. The data acquisition segment employs gradient pulses to encode internal displacement by means of

phase using a stimulated echo sequence. Internal displacements occur in response to an external deformation force synchronized to the acquisition sequence. By timing control, mechanical motion occurs while the relevant magnetization is longitudinal. The stimulated echo allows extension of the mechanical transition period to avoid potentially long-lived or ill-defined oscillations within the object such that an estimate of "static" displacement is achieved. Image registration or feature tracking (14) is not required because the object is in one deformation state for all spatial encoding.  $T_1$  relaxation and diffusion, which erode signal, ultimately set practical limits on this period. In these experiments, 200 to 350 msec was sufficient to allow static displacement measurement of rubber and gelatin/tissue phantoms using a simple air-bladder pneumatic system.

This arrangement required the object to "passively" recoil during the TM period. Clearly, a faster deformation system can be built using external forces to "actively" deform the object during the stimulated echo mixing period. A shorter mixing time would then be used yielding a larger signal.

To date, two approaches are present in elasticity imaging: static reconstructive elasticity imaging (25, 26) and dynamic shear-wave elasticity imaging (20, 21, 23). In both, an external static or dynamic deformation is applied while the resulting displacement/strain or propagating shear wave is detected using an imaging modality. In reconstructive elasticity imaging, the elasticity distribution must be reconstructed from static displacement and strain images. The ability to control the internal deformation pattern by varying the externally applied load, and high SNR displacement and strain estimates are the benefits of this method, although numerical reconstruction algorithms are required. Wherein the modeled assumptions are valid, these algorithms exist. For more general applications, they must be refined further. In shear-wave elasticity imaging, local shear wavelength measurements allow direct and simple calculation of the shear elastic modulus. However, the interference of shear waves reflected from any elasticity inhomogeneities within the tissue, along with attenuation of shear waves, and conversion between shear and bulk waves are challenges of this method.

In these experiments a displacement sensitivity of  $\Phi_d = 15.33 \pi/\text{mm}$  was achieved using moderate gradient factors. The ultimate quality of Young's modulus reconstruction depends on the induced phase shift, equal to

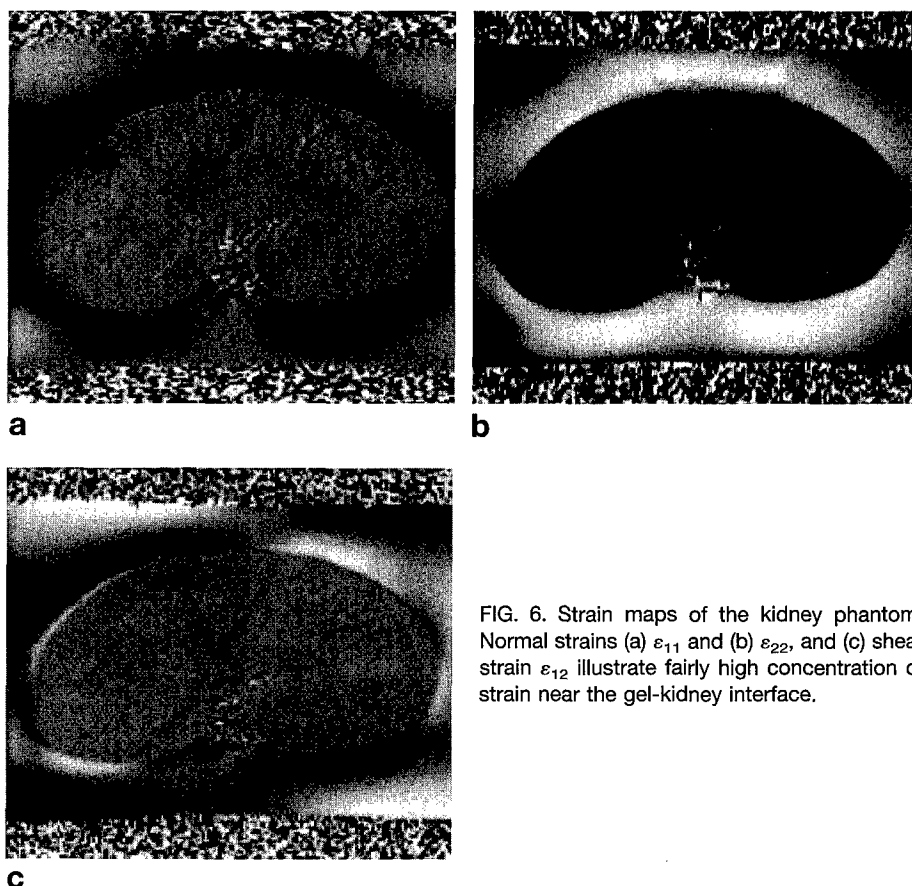


FIG. 6. Strain maps of the kidney phantom. Normal strains (a)  $\epsilon_{11}$  and (b)  $\epsilon_{22}$ , and (c) shear strain  $\epsilon_{12}$  illustrate fairly high concentration of strain near the gel-kidney interface.

the product of  $\Phi_d$  and local displacement. There is a limit, however, to the advantages gained by increasing phase shift. As spatial phase gradients become large, the phase distribution within a given voxel reduces signal amplitude. Assuming a linear phase distribution of range  $\beta$  with a voxel, the signal modulation function is given by  $\text{sinc}(\beta)$ . For illustration, consider the vertical phase excursion of  $21\pi$  observed across the 80-mm phantom in Fig. 2b. If the vertical phase excursion was evenly distributed across voxels, the phase range within each 0.78-mm voxel would be approximately  $0.2\pi$ . This implies a signal reduction factor of  $\text{sinc}(0.2\pi) = 0.94$  (i.e., signal loss of 6%). Clearly phase gradients can be more concentrated depending on object geometry, elastic heterogeneity, and deformation geometry. This concentration can lead to regions of significant signal loss in a manner analogous to flow dephasing in conventional MRI. Under such conditions, a smaller voxel size can (paradoxically) yield higher signal. In addition, inspection for significant signal loss within the displacement-sensitive magnitude image can identify high-strain regions near soft/hard interfaces of a lesion.

Water diffusion in the presence of displacement encoding gradients is another source of signal attenuation. We estimate the signal reduction factor for freely diffusing water was  $\approx 0.24$  in these experiments (i.e., 76% signal lost to diffusion effects). Diffusion effects are lessened by reducing  $\Phi_d$ , or alternatively by shortening TM without affecting  $\Phi_d$ . In either case, diffusion effects are assumed independent of the deformation state, and

therefore are ignored in the elasticity reconstruction. Because displacement phase shift is the product of local displacement and  $\Phi_d$ , the selection of  $\Phi_d$  is somewhat arbitrary as long as the applied differential deformation is adequate for elasticity reconstruction. In these preliminary experiments, the differential deformation was  $< 1.5$  mm across the imaged object. For multi-step acquisitions, as done here, good reproducibility of deformation is essential. Significant variation in deformation magnitude over the acquisition will lead to phase instability, motion-like artifact in base images, and errors that propagate through the elasticity reconstruction. It is a minor technical challenge to achieve relatively high displacement reproducibility in the deformation apparatus. Irreproducible motions that originate within the imaged object, however, can be problematic and are analogous to undesired physiologic motion artifacts

in *in vivo* diffusion MRI. Fortunately, unlike diffusion and physiologic motions, the targeted motion in elasticity imaging is externally driven. As such, the displacement amplitude in response to an external differential deformation can be significantly greater than irreproducible or asynchronous displacement. For many *in vivo* applications including the breast, increasing the differential deformation severalfold relative to that applied in these phantom studies can reduce motion artifact. Gradient factors and  $\Phi_d$  would be reduced accordingly, which would yield the added benefit of increased signal otherwise lost to diffusion effects.

In practice, the definition of a closed contour of constant Young's modulus within the tissue can be a challenge. A hybrid procedure can be used as detailed elsewhere (26) and summarized as follows. The strain images are first processed to highlight boundaries between regions of different elastic modulus. This procedure is based on the stress continuity property of continuous media such as tissue and can define regions of very small modulus variations. After this boundary detection, closed contours of small elasticity variations are defined. The modulus along the contours is considered constant, thereby providing the boundary condition for complete reconstruction of the elasticity within the region of interest based on numerical solution of Eq. [6]. The elasticity distribution reconstructed in this way is the modulus relative to the modulus along the boundary. For breast elasticity imaging, it is anticipated that such a contour can be defined *a priori* within the subcutaneous fat that surrounds breast parenchyma. As-

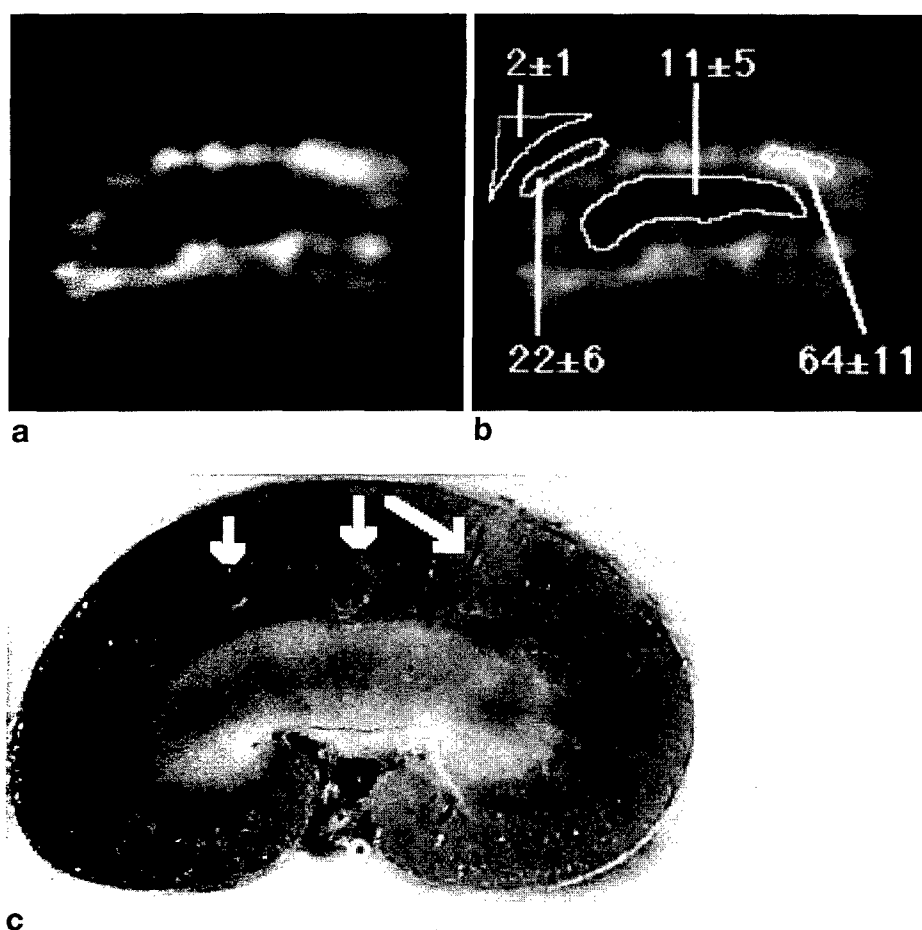


FIG. 7. (a) Reconstructed Young's modulus image within a rectangular  $94 \times 51$  mm region encompassing the kidney. (b) Relative Young's modulus for the scribed ROIs indicate high elastic modulus at the glutaraldehyde injection site in the upper-right quadrant of the kidney parenchyma. (c) The optical image of the kidney phantom approximately 20 h after MRI. Areas marked by arrows were noticeably harder as assessed by sense of manual touch.

suming the Young's modulus of the fat boundary is constant, the relative Young's modulus image of parenchyma can be reconstructed. Alternatively, the breast can be surrounded by a high-signal cuff of known elastic modulus and imaged. An image of absolute Young's modulus can then be reconstructed if the boundary contour is defined within the cuff material.

Some artifacts present in elasticity images (Figs. 4 and 7) are due to violation of the plane strain state approximation in these experiments. Indeed, if a plane strain state is not present, the reconstruction based on Eq. [6] will be in error. The elasticity reconstruction, however, does not have to be limited by a plane strain assumption if all 3D components of the displacement vector are available. Fortunately, such information would be available using 3D displacement encoding within a volumetric imaging sequence. The issue of long scan time could be resolved by incorporating echo-planar imaging or fast-spin-echo segments for spatial encoding. Correspondingly, an elasticity reconstruction based on Eq. [5] would be applied to produce volumetric elasticity maps.

The long-range goal of quantitative elasticity imaging is to provide remote palpation thus expanding its limited

range to include deep lying lesions. One application would be measurement of elasticity in breast tissue not accessible to manual palpation. *In situ* studies of Young's elastic modulus performed on samples of breast tissue indicate that there is a large difference in elastic modulus between normal and pathologically transformed breast tissues. Others have analyzed the Young's modulus differences between different soft tissues and have found 1–2 orders of magnitude difference in Young's elastic moduli of a tissue in different physiologic states (1). If elastic changes predate formation of calcifications, elasticity imaging could potentially increase detection and/or characterization of malignant breast masses and thus be an important addition to existing clinical diagnostic tools. Practical issues such as the relatively high cost of MRI may hinder use of this approach as a screening test. Nevertheless, additional work to define the role of this technique as a primary diagnostic tool or supplemental problem-solving modality in the management of soft-tissue disease is well justified.

## REFERENCES

1. A. P. Sarvazyan, A. R. Skovoroda, S. Y. Emelianov, J. B. Fowlkes, J. G. Pipe, R. S. Adler, R. B. Buxton, P. L. Carson, Biophysical Bases of Elasticity Imaging, in "Acoustical Imaging," volume 21, p. 223–240, Plenum Press, New York, 1995.
2. A. R. Skovoroda, A. N. Klishko, D. A. Gukasyan, E. I. Maevsky, V. D. Ermilova, G. A. Oranskaya, A. P. Sarvazyan, Quantitative analysis of the mechanical characteristics of pathologically altered soft biological tissues. *Biofizika* **40**, 1335–1340, (1995).
3. D. Hill, V. White, D. Jolley, K. Mapperson, Self examination of the breast: Is it beneficial? Meta-analysis of studies investigating breast self examination and the extent of disease in patients with breast cancer. *Br. J. Med.* **297**, 271–275 (1988).
4. P. A. Newcomb, S. Weiss, B. E. Storer, D. Scholes, B. E. Young, Breast self examination in relation to the occurrence of advanced breast cancer. *J. Natl. Cancer Inst.* **83**, 260–265 (1991).
5. R. J. Dickinson, C. R. Hill, Measurement of soft tissue motion using correlation between A-scans. *Ultrasound Med. Biol.* **8**, 263–271 (1982).
6. M. Tristram, D. C. Barbosa, D. O. Cosgrove, D. K. Nassiri, J. C. Bamber, C. R. Hill, Ultrasonic study of *in vivo* kinetic characteristics of human tissue. *Ultrasound Med. Biol.* **12**, 927–937 (1986).
7. M. Tristram, D. C. Barbosa, D. O. Cosgrove, J. C. Bamber, C. R. Hill, Application of Fourier analysis to clinical study of patterns of tissue movement. *Ultrasound Med. Biol.* **14**, 695–707 (1988).
8. R. M. Lerner, S. R. Huang, K. J. Parker, "Sono-elasticity" images derived from ultrasound signals in mechanically vibrated tissues. *Ultrasound Med. Biol.* **16**, 231–239 (1990).

9. K. J. Parker, S. R. Huang, R. A. Musulin, R. M. Lerner, Tissue response to mechanical vibrations for "sonoelasticity imaging." *Ultrasound Med. Biol.* **16**, 241-246 (1990).
10. K. J. Parker, R. M. Lerner, Sonoelasticity of organs: shear waves ring a bell. *J. Ultrasound Med.* **11**, 387-392 (1992).
11. J. Ophir, I. Cespedes, H. Ponnekanti, Y. Yazdi, X. Li, Elastography: a quantitative method for imaging the elasticity of biological tissues. *Ultrason. Imaging.* **13**, 111-134 (1991).
12. B. S. Garra, E. I. Cespedes, J. Ophir, S. R. Spratt, R. A. Zuurbier, C. M. Magnant, M. F. Pennanen, Elastography of breast lesions: initial clinical results. *Radiology* **202**, 79-86 (1997).
13. R. Adler, J. M. Rubin, P. Bland, P. Carson, Characterization of transmitted motion in fetal lung: quantitative analysis. *Med. Phys.* **16**, 333-337 (1988).
14. M. O'Donnell, A. R. Skovoroda, B. M. Shapo, S. Y. Emelianov, Internal displacement and strain imaging using ultrasonic speckle tracking. *IEEE Trans. Ultrason. Ferroelectrics and Frequency Control* **41**, 314-325 (1994).
15. S. Y. Emelianov, M. A. Lubinski, W. F. Weitzel, R. C. Wiggins, A. R. Skovoroda, M. O'Donnell, Elasticity imaging for early detection of renal pathologies. *Ultrasound Med. Biol.* **21**, 871-883 (1995).
16. L. Axel, L. Dougherty, Heart wall motion: improved method of spatial modulation of magnetization for MR imaging. *Radiology* **169**, 59-63 (1988).
17. E. A. Zerhouni, D. M. Parish, W. J. Rogers, A. Yang, E. P. Shapiro, Human heart: tagging with MR imaging - a method for noninvasive assessment of myocardial motion. *Radiology* **169**, 164-172 (1988).
18. N. J. Pelc, M. Drangova, L. R. Pelc, Y. Zhu, D. C. Noll, B. S. Bowman, R. J. Herfkens, Tracking of cyclic motion with phase-contrast cine MR velocity data. *J. Magn. Reson. Imaging* **5**, 339-345 (1995).
19. J. B. Fowlkes, S. Y. Emelianov, J. G. Pipe, A. R. Skovoroda, R. S. Adler, P. L. Carson, A. P. Sarvazyan, Magnetic resonance imaging techniques for detection of elasticity variation. *Med. Phys.* **22**, 1771-1778 (1995).
20. R. Muthupillai, D. J. Lomas, P. J. Rossman, J. F. Greenleaf, A. Manduca, R. L. Ehman, Magnetic resonance elastography by direct visualization of propagating acoustic strain waves. *Science* **269**, 1854-1857 (1995).
21. R. Muthupillai, P. J. Rossman, J. F. Greenleaf, S. J. Riederer, R. L. Ehman, MR imaging of acoustic strain waves: initial *in vivo* results, in "Proc., ISMRM, 4th Scientific Meeting and Exhibition, 1996," New York, p. 475.
22. D. B. Plewes, I. Betty, S. N. Urchuk, I. Soutar, Visualizing tissue compliance with MR imaging. *J. Magn. Reson. Imaging* **5**, 733-738 (1995).
23. D. B. Plewes, G. Poole, M. Leitch, S. N. Urchuk, MR assessment of the viscoelastic properties of tissue through the propagation of transient strain waves, in "Proc., ISMRM, 4th Scientific Meeting and Exhibition, 1996," New York, p. 476.
24. I. Cespedes, J. Ophir, H. Ponnekanti, N. Maklad, Elastography: elasticity imaging using ultrasound with application to muscle and breast *in vivo*. *Ultrason. Imaging* **15**, 73-88 (1993).
25. A. Skovoroda, S. Emelianov, M. Lubinski, A. Sarvazyan, M. O'Donnell, Theoretical analysis and verification of ultrasound displacement and strain imaging. *IEEE Trans. Ultrason. Ferroelectrics and Frequency Control* **41**, 302-313 (1994).
26. A. Skovoroda, S. Emelianov, M. O'Donnell, Tissue elasticity reconstruction based on ultrasound displacement and strain images. *IEEE Trans. Ultrason. Ferroelectrics and Frequency Control* **42**, 747-765 (1995).
27. S. Y. Emelianov, A. R. Skovoroda, M. A. Lubinski, M. O'Donnell, Reconstructive Elasticity Imaging, in "Acoustical Imaging," volume 21, p. 241-253, Plenum Press, New York, 1995.



DEPARTMENT OF THE ARMY  
US ARMY MEDICAL RESEARCH AND MATERIEL COMMAND  
504 SCOTT STREET  
FORT DETRICK, MARYLAND 21702-5012

REPLY TO  
ATTENTION OF:

MCMR-RMI-S (70-1y)

23 Aug 01

MEMORANDUM FOR Administrator, Defense Technical Information  
Center (DTIC-OCA), 8725 John J. Kingman Road, Fort Belvoir,  
VA 22060-6218


SUBJECT: Request Change in Distribution Statement

1. The U.S. Army Medical Research and Materiel Command has reexamined the need for the limitation assigned to the technical reports listed at enclosure. Request the limited distribution statement for these reports be changed to "Approved for public release; distribution unlimited." These reports should be released to the National Technical Information Service.

2. Point of contact for this request is Ms. Judy Pawlus at DSN 343-7322 or by e-mail at judy.pawlus@det.amedd.army.mil.

FOR THE COMMANDER:

Encl

  
PHYLIS M. RINEHART  
Deputy Chief of Staff for  
Information Management

Reports to be Downgraded to Unlimited Distribution

ADB241560	ADB253628	ADB249654	ADB263448
ADB251657	ADB257757	ADB264967	ADB245021
ADB263525	ADB264736	ADB247697	ADB264544
ADB222448	ADB255427	ADB263453	ADB254454
ADB234468	ADB264757	ADB243646	
ADB249596	ADB232924	ADB263428	
ADB263270	ADB232927	ADB240500	
ADB231841	ADB245382	ADB253090	
ADB239007	ADB258158	ADB265236	
ADB263737	ADB264506	ADB264610	
ADB239263	ADB243027	ADB251613	
ADB251995	ADB233334	ADB237451	
ADB233106	ADB242926	ADB249671	
ADB262619	ADB262637	ADB262475	
ADB233111	ADB251649	ADB264579	
ADB240497	ADB264549	ADB244768	
ADB257618	ADB248354	ADB258553	
ADB240496	ADB258768	ADB244278	
ADB233747	ADB247842	ADB257305	
ADB240160	ADB264611	ADB245442	
ADB258646	ADB244931	ADB256780	
ADB264626	ADB263444	ADB264797	